In vivo capture and label-free detection of early metastatic cells

Samira M. Azarin[1], **Ji Yi**[2], **Robert M. Gower**[3], **Brian A. Aguado**[2], **Megan E. Sullivan**[4], **Ashley G. Goodman**[5], **Eric J. Jiang**[5], **Shreyas S. Rao**[5], **Yinying Ren**[5], **Susan L. Tucker**[6], **Vadim Backman**[2,7,8,*], **Jacqueline S. Jeruss**[9,10,*], and **Lonnie D. Shea**[5,11,12,13,*]

[1]Department of Chemical Engineering and Materials Science, University of Minnesota, Minneapolis, MN 55455, USA

[2]Department of Biomedical Engineering, Northwestern University, Evanston, IL 60208, USA

[3]Department of Chemical Engineering, University of South Carolina, Columbia, SC 29208, USA

[4]Department of Pathology, Northwestern University Feinberg School of Medicine, Chicago, IL 60611, USA

[5]Department of Chemical and Biological Engineering, Northwestern University, Evanston, IL 60208, USA

[6]Department of Bioinformatics and Computational Biology, The University of Texas MD Anderson Cancer Center, Houston, TX, 77030, USA

[7]Chemistry of Life Processes Institute (CLP), Northwestern University, Evanston, IL 60208, USA

[8]The Robert H. Lurie Comprehensive Cancer Center of Northwestern University, Chicago, IL 60611, USA

[9]Department of Surgery, University of Michigan, Ann Arbor, MI 48105, USA

[10]Department of Obstetrics and Gynecology, Northwestern University, Chicago, IL 60611, USA

[11]Institute for BioNanotechnology in Medicine (IBNAM), Northwestern University, Chicago, IL 60611, USA

[12]Department of Biomedical Engineering, University of Michigan, Ann Arbor, MI 48105, USA

[13]Department of Chemical Engineering, University of Michigan, Ann Arbor, MI 48105, USA

*Address correspondence to Lonnie D. Shea (ldshea@umich.edu), Jacqueline S. Jeruss (jjeruss@umich.edu), or Vadim Backman (v-backman@northwestern.edu).

Abstract

Breast cancer is a leading cause of death for women, with mortality resulting from metastasis. Metastases are often detected once tumor cells affect the function of solid organs, with a high disease burden limiting effective treatment. Here we report a method for the early detection of metastasis using an implanted scaffold to recruit and capture metastatic cells *in vivo*, which achieves high cell densities and reduces the tumor burden within solid organs 10-fold. Recruitment is associated with infiltration of immune cells, which include Gr1^{hi}CD11b^{+} cells. We identify metastatic cells in the scaffold through a label-free detection system using inverse-spectroscopic optical coherence tomography, which identifies changes to nanoscale tissue architecture associated with the presence of tumor cells. For patients at risk of recurrence, scaffold implantation following completion of primary therapy has the potential to identify metastatic disease at the earliest stage, enabling initiation of therapy while the disease burden is low.

Introduction

The discovery of metastatic spread of a primary tumor is often associated with poor prognosis, owing to the fact that metastases typically go undetected until the function of one or more organs have been affected. Identification of metastasis prior to significant organ invasion would enable interventional strategies to halt disease progression while the disease burden is still low[1]. Much attention has been focused on screening for the presence of circulating tumor cells (CTCs) as a measure of metastasis. CTCs are present at low numbers in the blood, and technologies such as microfluidic devices have been designed to capture and quantify the number of CTCs from patient blood samples[2,3]. Recently, a system that also enables expansion of CTCs following capture has been developed[4]. These technologies provide opportunities for studying the biology of CTCs, development of biomarkers, disease monitoring, and personalized medicine strategies. However, CTCs can remain in the circulation for long periods of time before homing to and colonizing a metastatic site, with some tumor cells being shed at early points during tumor progression[5,6]. Thus, we sought to develop a method for capturing and detecting cells that have extravasated and colonized a site, which are steps in the metastatic cascade downstream from the circulation of tumor cells.

Paget's seed-and-soil hypothesis, developed a century ago, proposed that dissemination of cancer cells to specific sites in the body, such as lung or liver, is not random but rather is due to the receptive microenvironments at those sites[7]. More recently, studies have shown that prior to colonization of a metastatic site, a "pre-metastatic niche" is established by VEGFR1+ bone marrow-derived hematopoietic progenitor cells[8]. These cells create a tumor-supportive microenvironment comprised of several cell types, including hematopoietic and endothelial progenitor cells and immune cells, that condition the environment with matrix proteins, cytokines, and chemokines in order to facilitate migration, invasion, proliferation, and angiogenesis at the metastatic site[9–11]. Immune cells, in particular, play critical roles in homing and colonization of the metastatic site. Macrophages facilitate extravasation of metastatic cells as they begin the process of colonization[12]. Myeloid-derived suppressor cells[13–15] and inflammatory monocytes[16] have also been associated with metastatic sites, and neutrophils have been shown to facilitate

transendothelial migration of tumor cells. Importantly, the existence of the pre-metastatic niche indicates that a site could be engineered to recapitulate the microenvironment of the niche *in vivo*.

In this report, we develop a biomaterial implant to recruit and capture metastatic cells, combined with an imaging system utilizing IS-OCT for label-free detection of cancer cells at the implant, that together constitute a system to detect early metastases. The implants are microporous scaffolds composed of poly(lactide-co-glycolide) (PLG), a material that is FDA approved for a variety of applications. We also investigate if the capture of extravasating metastatic cells can reduce colonization of solid organs and consequently tumor burden, which could have therapeutic implications. Additionally, modulation of the local immune environment may be a versatile approach for recruiting tumor cells that is distinct from strategies that mimic the microenvironment of a target organ, such as bone[17,18]. To this end, the immune response at the implant, which consists of numerous cell types such as macrophages and neutrophils, is hypothesized to mediate recruitment of tumor cells[8,10,12,16,19,20], and this mechanism of recruitment is investigated through localized delivery of the chemokine CCL22 and transplantation of myeloid-derived suppressor cells. Recruited tumor-associated myeloid-derived suppressor cells, in part, contribute to the formation a pre-metastatic niche, which supports a permissive environment for the capture of tumor cells in the scaffold. This approach for immune cell-mediated capture and early detection of metastatic cells has the potential to be broadly applicable to many types of cancer.

Results

Scaffolds for *in vivo* capture of metastasizing cells

An orthotopic model of human breast cancer metastasis was employed to investigate the capture of metastatic cells at a biomaterial implant. tdTomato- and luciferase-expressing MDA-MB-231BR (231BR) cells, a highly metastatic variant of the MDA-MB-231 cell line[21], were transplanted into the right mammary fat pads of female NOD/SCID-IL2Rγ$^{-/-}$ (NSG) mice. One week after tumor inoculation, microporous PLG scaffolds (5 mm diameter, 2 mm height, Supplementary Fig. 1a–c) were implanted into the peritoneal fat pads, a site to which 231BR cells are not reported to colonize, yet supports the vascularization of PLG scaffolds. Bioluminescence imaging (BLI) and histological analysis of peritoneal fat pads removed 28 days after tumor inoculation demonstrated the presence of tumor cells within the implanted PLG scaffold (Fig. 1a,d) and the absence of tumor cells in fat pads without scaffolds (Fig. 1b,e), indicating that the local environment generated by implantation of the scaffold enabled recruitment of metastatic cells. Primary tumor growth was not affected by either implantation of scaffolds or a mock surgery (Supplementary Fig. 2). Staining for fibronectin, a matrix protein reported to be involved in establishment of the pre-metastatic niche[8], indicated that fibronectin was present in scaffolds implanted in both healthy and tumor-bearing mice as early as 7 days post-implantation (Supplementary Fig. 1d). Interestingly, recruitment of cells to the scaffold was not site-specific, as tumor cells were detected in scaffolds implanted in the subcutaneous tissue (Supplementary Fig. 3).

Scaffolds reduce tumor burden in solid organs

We subsequently investigated whether capturing tumor cells in scaffolds would reduce colonization of standard metastatic sites, such as the lung and liver. At 28 days post-tumor inoculation, the relative abundance of tumor cells, reported as the ratio of tdTomato-positive tumor cells to total cells, was determined. For mice that received scaffolds, the relative abundance of tumor cells in the lung was 1:5,400, compared to 1:645 for mice receiving a mock surgery (Fig 2a, Supplementary Fig. 4). Thus, the presence of a scaffold reduced the tumor burden for the lung by $88 \pm 7\%$ (average $\pm$ SEM). Histological analysis of lung sections confirmed a reduction in the tumor cell burden with scaffold implantation (Fig. 2b,c), with an average of 1.7 ± 0.5 metastatic lesions per section observed in the lungs of scaffold-bearing mice, compared to 5.5 ± 1.7 lesions per section in mice receiving mock surgeries. Furthermore, flow cytometric analysis of cells isolated from the liver showed detectable tumor cells in 8 out of 8 mice receiving mock surgeries, while mice receiving scaffold implants only exhibited detectable tumor cells in 2 of 8 livers (P < 0.01, Fisher's exact test).

Early detection of tumor cells in scaffold

The potential to use scaffolds for early detection of metastasis was determined by quantifying the percentage of tumor cells in intraperitoneal and subcutaneous scaffolds compared to the lung and liver at day 14 post-tumor inoculation. In a group of eight mice, most intraperitoneal scaffolds (15/16) contained tumor cells at this time point, while none of the mice had detectable tumor cells in the lung and liver (Fig. 3a). In a separate group of mice, all subcutaneous scaffolds (10/10) contained tumor cells. The incidence of detectable metastatic disease at this early time point was lower than at day 28 post-tumor inoculation. At day 28 post tumor inoculation in scaffold-bearing mice, the lung and liver exhibited tumor cells in 8 and 2 of the 8 mice, respectively. Furthermore, for mice receiving mock surgeries instead of scaffold implants, the incidence of metastatic cells in both the lung and liver increased to 8 out of 8 mice. Importantly, at day 14 post-inoculation, while none of the lungs and livers exhibited detectable tumor cells, both intraperitoneal and subcutaneous scaffolds had a detectable percentage of tumor cells ($0.019 \pm 0.005\%$ for intraperitoneal scaffolds and $0.044 \pm 0.017\%$ for subcutaneous scaffolds) (Fig. 3b, Supplementary Fig. 5). This ability to detect tumor cells in the scaffold prior to detection in the lungs and liver may enable the early detection of metastatic disease through imaging the scaffold.

Label-free detection of metastasis at the scaffold

Inverse spectroscopic optical coherence tomography (IS-OCT)[22] was applied to directly visualize the scaffold architecture and provide quantitative measurement of the ultrastructural changes induced by the cancer cells. IS-OCT is a light scattering-based technique capable of non-invasive 3-D imaging of tissue morphology with micron-level resolution and millimeter-level penetration depth[23,24]. In addition, for each 3-D resolution voxel ($15 \times 15 \times 2$ μm) IS-OCT also performs a spectroscopic analysis and quantifies the power of the spectra by a scattering model $I(\lambda) \propto \lambda^{D-4}$ [22]. D is the shape factor that physically defines the macromolecular density correlation function for a range of length scales from ~40 nm to 350 nm[25], with higher D values indicating a more clumped structure. It has been

demonstrated that D is a ubiquitous marker of the ultrastructural alterations in the early stages of various cancer types[26–30], with both neoplastic cells and the surrounding stroma exhibiting an increase in D in part due to chromatin condensation and collagen remodeling, respectively[27,30,31]. Given the nanoscale sensitivity of measuring D and the tissue-level imaging capability, we hypothesized that IS-OCT could be an effective approach for detection of cancer cells within the scaffold.

In vitro studies were performed to demonstrate that IS-OCT could capture changes in D for cells and matrices, and the technique was subsequently applied to *in situ* imaging of scaffolds. IS-OCT analysis of 231BR cell pellets confirmed that they had a higher D than normal mammary epithelial cells (MCF10A) and cells isolated from lungs of tumor-free NSG mice (3.49 ± 0.12, 2.74 ± 0.15, and 3.00 ± 0.13, respectively, Supplementary Fig. 6a). Changes to collagen remodeling by 231BR cells were evaluated by culturing 231BR cells in collagen gels for 3 days, after which cells were extracted and the gels were analyzed using IS-OCT. 231BR-conditioned matrices exhibited a D value of 1.69 ± 0.08 compared to a D value of 1.29 ± 0.04 for gels cultured with media (Supplementary Fig. 6b). With confirmation of the technique *in vitro*, *in situ* IS-OCT analysis was applied to scaffolds, which demonstrated that scaffolds implanted in the subcutaneous tissue of tumor-bearing mice also had an increase in D at day 14 post-tumor inoculation compared to control scaffolds in tumor-free mice (Fig. 4), with an average D value of 5.77 ± 0.38 in tumor-bearing mice compared to 4.71 ± 0.17 in tumor-free mice. This increase in D is consistent with the changes associated with the presence of cancerous cells and the ensuing reorganization of the extracellular matrix. These results indicate that this method can be used for label-free detection of micrometastases within the scaffold at the early stages of metastatic disease.

Immune cells contribute to tumor cell recruitment

Given the critical role of various immune cells types in establishing the pre-metastatic niche[8,10,12,16,19,20], we hypothesized that the immune response to the scaffold was mediating recruitment of tumor cells. For analysis of the immune environment within the scaffolds, we utilized an immune-competent mouse model in addition to the NSG model in order to account for effects of both the innate and adaptive immune response. Scaffolds implanted into BALB/c mice inoculated with 4T1 mouse breast cancer cells also demonstrated metastatic cells within the scaffold, indicating that the scaffold could still achieve homing within the context of an intact immune system (Supplementary Fig. 7).

Inflammatory cells proposed to be involved in recruiting tumor cells were characterized within the peritoneal fat pads of mice in the presence and absence of a scaffold. A high density of CD45-positive leukocytes was present in histological sections of the scaffold, with no observed CD45-positive leukocytes present in fat pads of mice receiving mock surgeries (Fig. 5a,b). The ability of CD45-positive leukocytes to influence homing of tumor cells was investigated through migration assays using media conditioned by splenocytes isolated from spleens of tumor-bearing mice, as the spleen contains a large number of immune cells and has a distribution of immune cells similar to the scaffolds, with the predominant cell type being Gr1^{hi}CD11b^{+} cells (Supplementary Fig. 8). Migration of both

cell types was significantly increased in the presence of splenocyte-conditioned media relative to unconditioned media (Fig. 5c,d), with 261 ± 35 migrating 231BR cells per well in conditioned media compared to 137 ± 20 cells in unconditioned media and 521 ± 22 migrating 4T1 cells per well in conditioned media compared to 292 ± 23 cells in unconditioned media. These results indicate that paracrine signaling from immune cell populations similar to those present in the scaffold can induce migration of tumor cells.

Before and after the introduction of cancer cells, we analyzed the local immune environment of the implanted scaffold, which was compared to that of the lung, a common site of breast cancer metastasis. Flow cytometric analysis demonstrated that during disease progression, the most notable change in the relative distribution of immune cells was an increase in $Gr1^{hi}CD11b^+$ cells (Fig 5e–h, Supplementary Fig. 9–11). This increase was consistent in both the NSG and BALB/c mouse models, and was found in both the lungs and scaffolds. In the lungs of the NSG mice, the percentage of $Gr1^{hi}CD11b^+$ cells increased from $45 \pm 2\%$ at day 0 (no cancer cells) to $52 \pm 3\%$ at day 14-post cancer cell inoculation, to $84 \pm 1\%$ at day 28 post cancer cell inoculation (Fig 5e), Following this trend, the percentage of $Gr1^{hi}CD11b^+$ cells found in the scaffolds from the NSG mice increased from $21 \pm 1\%$ (tumor-free mice), to $35 \pm 5\%$ at day 14 post cancer cell inoculation, to $62 \pm 2\%$ at day 28 post cancer cell inoculation (Fig 5g). In the lungs of BALB/c mice, $Gr1^{hi}CD11b^+$ cells increased from $1 \pm 0.1\%$ at day 0 (tumor-free mice) to $57 \pm 1\%$ at day 14-post cancer cell inoculation, to $89 \pm 2\%$ at day 28-post cancer cell inoculation (Fig. 5f). Likewise, within the scaffolds from the BALB/c mice, $Gr1^{hi}CD11b^+$ cells increased from $0.1 \pm 0.01\%$ (no cancer cells) to $32 \pm 3\%$ at day 14-post cancer cell inoculation, to $66 \pm 5\%$ at day 28-post cancer cell inoculation (Fig. 5h). These results highlight the correlation between disease exposure time and the relative abundance of $Gr1^{hi}CD11b^+$ cells found in both the lungs and scaffolds of affected animals, and show that the immune environment within a metastatic organ site is similar to that of an implanted scaffold.

We subsequently investigated the hypothesis that modulation of the inflammatory microenvironment within the scaffold site would influence recruitment of metastatic cells. Lentiviral vectors were delivered from the scaffold to promote localized transgene expression for the duration of the study (Supplementary Fig. 12). The chemokine CCL22 was selected for expression as it induces migration of splenocytes harvested from NSG mice (Supplementary Fig. 13a) yet does not influence the migration of tumor cells (Supplementary Fig. 13b). Flow cytometric analysis of CCL22 scaffolds at day 7 post-implantation indicated an increase in $Gr1^{hi}CD11b^+$ cells, which have been implicated in the pre-metastatic niche[10,14,15], from $20 \pm 2\%$ to $29 \pm 3\%$ in NSG mice and from in $14 \pm 1\%$ to $19 \pm 1\%$ BALB/c mice (Fig. 6a,c). Additionally, $F4/80^+CD11b^+$ inflammatory macrophages, which are recruited to circulating metastatic cells as they undergo extravasation and begin colonization[12], increased from $28 \pm 2\%$ to $34 \pm 2\%$ in the NSG model and from $10 \pm 1\%$ to $14 \pm 1\%$ in the BALB/c model (Fig. 6a,c). Furthermore, CCL22 expression increased the number of tdTomato-positive tumor cells present in the scaffold in both mouse models at day 7 post-implantation (day 14 post-tumor inoculation), with an average of 92 ± 16 cells compared to an average of 23 ± 4 cells for β-galactosidase expression in NSG mice and an average of 62 ± 5 cells compared to an average of 20 ± 2 cells for β-galactosidase expression in BALB/c mice (Fig. 6b,d).

A cell population upregulated by CCL22 delivery, $Gr1^{hi}CD11b^+$ cells, was next transplanted on the scaffold to directly modulate the local immune environment and further demonstrate that the immune environment mediates metastatic cell recruitment. $Gr1^{hi}CD11b^+$ $Gr1^{hi}CD11b^+$ cells were selected for these studies given their established role in the pre-metastatic niche, along with migration assays showing soluble factors secreted by MDSCs isolated from spleens of tumor-bearing NSG mice induced migration of 231BR cells (Fig. 6e). Interestingly, the $Gr1^{hi}CD11b^+$ cells induced migration to a greater extent than splenocyte-conditioned media (Supplementary Fig. 14). Implantation of scaffolds seeded with $Gr1^{hi}CD11b^+$ cells significantly increased the percentage of $Gr1^{hi}CD11b^+$ cells in the total leukocyte population (from $20 \pm 2\%$ to $26 \pm 2\%$, Fig. 6f) as well as the number of tumor cells (from 29 ± 10 to 74 ± 13 cells, Fig. 6g) present per scaffold, indicating that $Gr1^{hi}CD11b^+$ cells contributed to recruitment of tumor cells to the scaffold.

Discussion

This study demonstrates a platform technology for the capture and label-free detection of cancer cells early in the onset of the metastatic process. Biomaterial scaffolds were engineered to recruit metastatic cells *in vivo* through modulation of the local immune environment, with detection of cancer cells based on the tissue nanoarchitecture by IS-OCT. The ability of the scaffolds to reduce tumor burden in host organs that are standard sites of breast cancer metastasis suggests the potential use of the scaffold as a therapeutic tool, serving as a sink to capture circulating tumor cells. As opposed to models that employ tail vein injections to study lung colonization by directly placing large numbers of tumor cells in the bloodstream[32], the orthotopic model employed in this study more closely mimics the release of metastatic cells from the primary tumor observed in the clinical setting. The ability of the scaffolds to capture a fraction of the metastatic cells early in disease progression and consequently limit colonization to other organ sites is also a distinguishing feature from purely diagnostic approaches, such as the detection of circulating tumor cells in blood samples. Furthermore, cancer cells can be retrieved from scaffolds and analyzed for biomarkers unique to the metastatic setting, and targeted therapies could then be developed that are appropriately tailored to metastatic cancer cell biology.

The approach of designing scaffolds to capture circulating cells *in vivo* has been utilized for cancer as well as regenerative medicine applications. Strategies to develop biomaterial implants that capture endothelial progenitor cells and smooth muscle progenitor cells from the bloodstream have been implemented to promote vascularization of the implant[33–35]. Additionally, biomaterial scaffolds designed to recruit endogenous stem cells have promoted bone regeneration[36] and cardiac repair[37]. Strategies to capture circulating cancer cells *in vivo* have focused on mimicking the microenvironment of a target organ, as demonstrated by the use of scaffolds that mimic the bone microenvironment for capture of breast cancer cells[18] and hematopoietic cancer cells[17]. This technology utilized a broader approach of recruiting metastasizing breast cancer cells through local immune modulation, as immune cells have been shown to play critical roles in recruiting metastatic cells[9,10,12,14–16,19]. Given the importance of immune cells in regulating metastasis for several cancers, this approach may provide a more versatile method for capture of extravasating cancer cells *in*

vivo. Further, the coupling of cell capture strategies with label-free imaging methods (i.e., IS-OCT) demonstrates the potential for utilizing this approach as a diagnostic tool.

These scaffolds also provide an enabling tool to control the cell types and signals present at a local site in order to identify regulators of early events in colonization, which could lead to novel therapeutic targets for prevention of metastasis. The microenvironment within the scaffolds can be modified through cell transplantation, presentation of extracellular matrix proteins, or delivery of proteins or gene therapy vectors[38–41], and represents a platform for molecularly dissecting the biological cues that underlie the recruitment of metastatic cells. Herein, Gr1^{hi}CD11b$^+$ cells were either recruited through chemokine expression or transplanted on the scaffold, which enhanced recruitment of extravasating tumor cells. Gr1^{hi}CD11b$^+$ cells accumulate in the spleen during tumor progression[42], and previous reports indicate they are recruited to a pre-metastatic niche by inflammatory chemokines.[43] While the increase in Gr1^{hi}CD11b$^+$ cells in the scaffold was modest, the increase in cancer cells was substantial, which is consistent with multiple effects of Gr1^{hi}CD11b$^+$ cells on tumor cells[44].

Finally, scaffolds, coupled with IS-OCT imaging, functioned as a sensor to detect tumor cells early in the onset of metastatic progression, which could enable therapeutic intervention while the disease burden is low. While whole-body imaging techniques do not provide the requisite sensitivity and resolution to detect a few cells as they colonize a metastatic site, optical imaging is suited for this application. Optical coherence tomography (OCT) conventionally has been used to provide microscopic reconstruction of tissue morphology with a spatial resolution on the order of several microns. Accordingly, OCT has been applied to *in vivo* imaging of the tumor microenvironment[45]. IS-OCT models tissue as a medium with a continuously fluctuating macromolecular mass density[46]. By measuring its optical properties, the mass density correlation function can be inversely recovered at each 3-D voxel of spatial resolution[22]. Moreover, because IS-OCT utilizes the spectral information to measure the self-interference within a resolution-limited voxel, the length scale of sensitivity of ISOCT can be as small as ~35nm, far beyond the resolution limit of conventional microscopy[47–49]. While the necessary penetration depth and large volume of a solid organ such as the lung or liver would not be well-suited for IS-OCT-based detection of a small number of colonizing cells, the scaffold concentrates metastatic cells in an area beneath the skin, a site that is more readily accessible for imaging. Thus, IS-OCT provides a robust approach for identifying the changes to the scaffold microenvironment upon colonization by metastatic cells. Taken together, the early detection, reduced burden of metastatic disease, and potential to apply targeted therapies afforded by this technology could significantly extend the time to disease progression.

Methods

Study Design

The objective of the study was to utilize biomaterials scaffolds and optical imaging techniques in order to capture and detect metastasizing breast cancer cells *in vivo*. We hypothesized that due to the local inflammatory response following implantation, the scaffolds become infiltrated with immune cells conducive to recruiting metastatic cells, and

that a light scattering-based imaging method could detect changes to the tissue ultrastructure associated with arrival of the cancer cells. Animal studies were performed with at least 2 independent replicates of 4 to 8 female 10 to 14 week old mice per group with random assignment. Tissues were analyzed at day 14 or 28 post-tumor inoculation, with day 14 being the earliest timepoint for detecting metastasis and day 28 being the final timepoint, as the primary tumor reached the maximum allowable size. *In vitro* experiments had multiple samples that were independently repeated at least 2 times.

Tumor inoculation and volume measurement

Animal studies were performed in accordance with institutional guidelines and protocols approved by the Northwestern University Institutional Animal Care and Use Committee (IACUC). Tumor inoculation was performed by injecting 2×10^6 231BR (Northwestern University Developmental Therapeutics Core) or 4T1 (ATCC) cells in a volume of 50 μL PBS (Life Technologies) into the number four right mammary fat pads of 10–14 week old female NSG or BALB/c mice. NSG mice were purchased from The Jackson Laboratory or bred in house. BALB/c mice were purchased from The Jackson Laboratory. Tumor length and width were measured weekly using digital calipers (VWR) beginning at day 14 post-inoculation, and tumor volume was calculated using the formula Volume = (Width$^2 \times$ Length)/2.

Scaffold fabrication and implantation

Poly(lactide-co-glycolide) (PLG) scaffolds were fabricated as previously described[40]. Briefly, microspheres were prepared by emulsifying a 6% solution of PLG (Lakeshore Biomaterials; 75:25 lactide:glycolide, i.v. = 0.76 dL/g) in dicholoromethane in 1% poly(vinyl alcohol) (PVA). Microspheres were washed four times with deionized water to remove residual PVA and lyophilized overnight. Next, microspheres were mixed with 250–425 μm salt particles in a 30:1 ratio and pressed in a steel die at 1500 psi. The scaffolds were then gas-foamed and salt particles were removed by washing in water for 90 minutes. Scaffolds were sterilized with 70% ethanol and rinsed with water before drying. Incorporation of a viral vector was performed by incubating 1×10^9 viral particles in a volume of 10 μL PBS with the scaffold for 8 minutes. In these studies, tumors were inoculated at day 0 and scaffolds were implanted in the intraperitoneal fat pads or subcutaneous space at day 7.

Virus production

The lentiviral vector of interest was co-transfected with the packaging vectors pRSV-Rev, pIVS-VSV-G, and pMDL-GagPol[50] into HEK-293T cells grown in DMEM (Sigma) containing 10% fetal bovine serum (Life Technologies) for virus production using Lipofectamine 200 (Life Technologies). After 48 hours the supernatant was collected. Viral particles were concentrated using PEG-it (Systems Biosciences) and resuspended in PBS. Virus titer was quantified using the qPCR Lentivirus Titration Kit (Applied Biological Materials) according to the manufacturer's instructions.

Bioluminescence imaging

Five minutes prior to imaging, mice were injected IP with D-luciferin (Molecular Imaging Products; 20 mg/mL in PBS) at 150 mg/kg body weight. For whole animal imaging, mice were anesthetized with inhaled isoflurane and *in vivo* luciferase expression was evaluated using the IVIS Spectrum imaging system (Caliper Life Sciences). For imaging of tissues, mice were euthanized five minutes after injection with D-luciferin and tissues were retrieved and imaged using the IVIS Spectrum.

Histological analysis and immunohistochemistry

Organs and implanted scaffolds were retrieved from mice, rinsed in PBS and then immediately flash-frozen in pre-chilled isopentane. The frozen tissue was then embedded in optimal cutting temperature (OCT; Cardinal Health) compound with 30% sucrose. The lungs were sectioned at 12 μm, and the scaffolds and fat pads were sectioned at 14 μm thick sections using a cryostat (Microm HM 525; Microm International) and stored at −20 °C until staining. In order to determine the presence of tumor cells, slides were fixed with 4% paraformaldehyde (Sigma) for 10 minutes and stained with Gill III Hematoxylin (Leica) and Eosin Y (Leica). Blinded scoring of the number of tumor clusters in each tissue section was performed by a pathologist. Two sections were analyzed per mouse, and in each of 2 separate experiments, sections from 3 mice per group were analyzed, for a total of 6 animals per condition. The sections analyzed were non-adjacent and separated by at least 5 mm. For immunohistochemistry, sections were fixed for 12 minutes in 4% paraformaldehyde and stained with a polyclonal rabbit anti-CD45 primary antibody (1:100, Abcam) followed by a CF633 anti-rabbit secondary antibody (1:500, Sigma) or a polyclonal rabbit anti-fibronectin antibody (1:250, Abcam) followed by an Alexa Fluor® 488 anti-rabbit secondary antibody (1:500, Life Technologies). Nuclei were labeled with Hoechst 33250 (1:2000, Invitrogen). Samples were imaged using a Leica SP5 II laser scanning confocal microscope.

Flow cytometry

Mice were euthanized and tissues were retrieved, minced with microscissors in a 0.38 mg/mL solution of Liberase TL or TM (Roche Applied Science) in Hank's Balanced Salt Solution (HBSS; Life Technologies) and placed at 37 °C for 20 minutes. Liberase was neutralized with 0.125M EDTA, and cells were isolated by passing the digested tissue through a 70 μm filter (BD Biosciences) and rinsing with FACS buffer, PBS containing 0.5% Bovine Serum Albumin (BSA; Sigma) and 2mM EDTA (Life Technologies). Red blood cells were lysed using ACK lysing buffer (Life Technologies). For analysis of tdTomato-positive tumor cells, samples were resuspended in FACS buffer and analyzed using an LSR II flow cytometer (Becton Dickinson Immunocytometry Systems, BDIS). A standard curve was established for each organ by adding defined numbers of tumor cells into cells isolated from healthy lungs and livers and measuring the number of tdTomato-positive cells via flow cytometry. From this analysis, it was determined that the threshold tumor cell density of 0.002% (5 tumor cells in 250,000 total cells) was consistently and significantly above background, and thus samples were deemed to have detectable cancer cells if the tumor cell density was above 0.002%. For analysis of leukocyte populations, cells were blocked with anti-CD16/32 (1:50, eBioscience) and stained for viability using fixable blue

dead cell stain kit (Life Technologies). Cells were then stained with Alexa Fluor® 700-conjugated anti-CD45 (30-F11, 1:125; Biolegend), Pacific Blue-conjugated anti-Gr-1 (RB6-8C5, 1:70; Biolegend), FITC-conjugated anti-Ly-6C (HK1.4, 1:100; Biolegend), PE-Cyanine7-conjugated anti-F4/80 (BM8, 1:70; Biolegend), APC-conjugated anti-CD11c (N418, 1:85; eBioscience), v500-conjugated anti-CD11b (M1/70, 1:100; BD Biosciences), Pacific Blue-conjugated anti-CD19 (6D5, 1:100; Biolegend), v500-conjugated anti-CD4 (RM4-5, 1:100; BD Biosciences), FITC-conjugated anti-CD8a (53-6.7, 1:25; Biolegend), and PE-Cyanine7-conjugated anti-CD49b (DX5, 1:40; Biolegend). Samples were analyzed using an LSRFortessa flow cytometer (BDIS).

Splenocyte isolation for transplants and media conditioning

Spleens were isolated from tumor-bearing mice, minced using microscissors, and incubated in a 0.38 mg/mL solution of Liberase TL (Roche Applied Science) for 20 minutes at 37 °C. The minced tissue was passed through a 70 μm strainer and red blood cells were lysed using ACK lysing buffer (Life Technologies). To collect myeloid-derived suppressor cells (MDSCs), splenocytes were labeled with FITC-conjugated anti-Gr-1 (RB6-8C5, 1:100; Biolegend), APC-conjugated anti-Ly-6C (HK1.4, 1:50; Biolegend), and APC-eFluor780-conjugated anti-CD11b (M1/70, 1:100; eBioscience), and the $Gr1^{hi}CD11b^+Ly6C^-$ population was collected via FACS sorting using a BD FACSAria cytometer (BDIS). The remaining splenocyte population ($Gr1^{hi}CD11b^+$ cell-depleted) was also collected. For cell transplantation studies, scaffolds were rinsed with RPMI medium (Life Technologies) containing 5% fetal bovine serum (FBS; Life Technologies) and dried on gauze. 1×10^6 $Gr1^{hi}CD11b^+$ cells were seeded onto each scaffold in a volume of 5 μL RPMI with 5% FBS and scaffolds were implanted into the IP fat pads. For generation of conditioned media, splenocytes, $Gr1^{hi}CD11b^+$ cells, and $Gr1^{hi}CD11b^+$ cell-depleted splenocytes were each plated at a concentration of 1×10^6 cells/mL in RPMI media. Media was conditioned for 48 hours, after which the media was sterile-filtered to remove splenocytes.

Splenocyte migration assays

Migration assays were performed in 24-well Transwell chambers with 5 μm pore size filters (Corning). 1×10^6 splenocytes were placed in the top chamber in 100 μL of RPMI medium containing 10% FBS. 600 μL of RPMI medium containing 10% FBS with or without 200 ng/mL recombinant mouse CCL22 (Peprotech) was placed in the bottom chamber. After 1.5 hours, the number of cells that had migrated to the bottom chamber was counted using a hemocytometer.

Tumor cell migration assays

Tumor cells were serum-starved overnight in DMEM (Sigma) or RPMI (Life Technologies) containing 0.2% FBS (Life technologies). Migration assays were performed in 24-well Transwell chambers with 8 μm pore size filters (Corning). 5×10^4 231BR or 4T1 cells were placed in the top chamber in 300 μL of DMEM (for CCL22 assays) or RPMI (for conditioned media assays) containing 0.2% FBS. For CCL22 assays, 750 μL of DMEM containing 0.2% FBS with or without 200 ng/mL recombinant human CCL22 (Peprotech) was placed in the bottom chamber. For conditioned media, 750 μL of RPMI, splenocyte-conditioned RPMI, $Gr1^{hi}CD11b^+$ cell-conditioned RPMI, or RPMI conditioned with

Gr1^{hi}CD11b^{+} cell-depleted splenocytes was placed in the bottom chamber (all media was supplemented with 0.2% FBS). After 24 hours, the cells on the top of the filter were removed by gently scrubbing with a cotton swab, and the cells on the bottom of the filter were stained for 60 minutes in a 0.5% (*w/v*) solution of crystal violet (Sigma) in 60% PBS/40% ethanol. The inserts were rinsed in PBS and the number of migrating cells was counted.

Conditioning collagen gels with 231BR cells

A 1.6 mg/mL collagen I solution was prepared by mixing rat tail Collagen I (BD Biosciences) with deionized water, 10X PBS (Sigma, 1:10 dilution) and 1 N NaOH (Sigma, 1:1000 dilution) on ice. Collagen solution (150 μL) was placed in each well of a 48-well plate. Gels were incubated at 37 °C for 1 hour, after which 1.875E5 231BR cells in 400 μL of RPMI containing 10% FBS were seeded onto each gel. Control gels received 400 μL of RPMI containing 10% FBS. After incubation at 37 °C for 3 days, cells were extracted from the gels. The media was removed from each well and the gels were washed 3 times with 1X PBS (Life Technologies). A 20mM NH$_4$OH solution containing 0.5% (v/v) Triton X-100 (Sigma) was added to each well and the chamber slide was incubated at 37 °C for 5 minutes. After removal of the NH$_4$OH/Triton X-100 solution, the gels were washed twice with distilled water and twice with PBS. 175 μL of PBS was added to each well prior to imaging.

Scanning Electron Microscopy

Structural characteristics of scaffolds were imaged with a scanning electron microscope (Hitachi s4800-II cFEG SEM; Hitachi High-Technologies Corp.). A 15-nm gold coating was applied and the microscope was operated at 2 kV.

IS-OCT imaging and analysis

The OCT system used a Fourier domain configuration. A supercontinuum light source (NKT photonics, SuperK versa) provided a broadband laser from ~500 nm to 840 nm. The spectral range from 650 nm to 830 nm was used for OCT image construction. The laser was delivered by an optical fiber, collimated by a lens, and input into a cube beam splitter (BS; Thorlabs, CM1-BS013), by which the light was divided into a sample arm and a reference arm. The reference arm consisted of a series of glass plates for dispersion control and a mirror reflecting the light backward. The sample arm consisted of a two-dimensional scanning mirror (Thorlabs, GVSM002) and an objective lens (effective NA = 0.04; Zeiss) to focus the light onto specimens. The lateral resolution is estimated as 15 μm. The interfered light from the reference and sample arm at the BS was collected by another optical fiber and delivered to the spectrometer for spectral acquisition. The mirror was scanning at a frequency of 2.56 kHz, and a 3D acquisition lasted 25.6 s with 256 by 256 pixels in two lateral directions. The camera exposure time was 0.3 ms. With the bandwidth, the axial resolution was estimated as 2 μm.

The depth structural reconstruction was created by the following steps. The recorded spectrum was first normalized by the source spectrum, and then resampled into *k* domain with equal interval, and finally a Fourier transform was taken to recover the depth signal. *k* is the wave number, defined by k = $2\pi/\lambda$. The calculation of *D* value was performed by the

following steps. A Gaussian window with width $k_w = 0.36$ μm^{-1} was applied on the spectrum, and the depth structural reconstruction process was performed. This process was then repeated with the Gaussian window scanning through the whole spectral range, and the wavelength-dependent 3-D structure was obtained. The reduced range of spectrum relaxed the axial resolution to be about 20 μm. The averaged spectra from the specimen were modeled by $I(k) = k^{2-D/2}$. The value of D was then obtained by calculating the power of the spectra.

Statistical analysis

Data are presented as mean ± standard error (SEM), and p-values were determined using a Mann-Whitney test for single comparisons. For comparison of relative numbers of mice containing metastasis to various tissues, a Fisher's exact test was used to determine the p-value. Statistical analysis was performed using GraphPad Prism.

Supplementary Material

Refer to Web version on PubMed Central for supplementary material.

Acknowledgments

References

1. Griffith OL, Gray JW. 'Omic approaches to preventing or managing metastatic breast cancer. Breast Cancer Res. 2011; 13:230. [PubMed: 22216753]

2. Nagrath S, et al. Isolation of rare circulating tumour cells in cancer patients by microchip technology. Nature. 2007; 450:1235–1239. [PubMed: 18097410]

3. Stott SL, et al. Isolation of circulating tumor cells using a microvortex-generating herringbone-chip. Proc Natl Acad Sci USA. 2010; 107:18392–18397. [PubMed: 20930119]

4. Yoon HJ, et al. Sensitive capture of circulating tumour cells by functionalized graphene oxide nanosheets. Nat Nanotechnol. 2013; 8:735–741. [PubMed: 24077027]

5. Bednarz-Knoll N, Alix-Panabieres C, Pantel K. Clinical relevance and biology of circulating tumor cells. Breast Cancer Res. 2011; 13:228. [PubMed: 22114869]

6. Lacroix M. Significance, detection and markers of disseminated breast cancer cells. Endocr Relat Cancer. 2006; 13:1033–1067. [PubMed: 17158753]

7. Paget S. The distribution of secondary growths in cancer of the breast. 1889. Cancer Metastasis Rev. 1989; 8:98–101. [PubMed: 2673568]

8. Kaplan RN, et al. VEGFR1-positive haematopoietic bone marrow progenitors initiate the pre-metastatic niche. Nature. 2005; 438:820–827. [PubMed: 16341007]

9. Erler JT, et al. Hypoxia-induced lysyl oxidase is a critical mediator of bone marrow cell recruitment to form the premetastatic niche. Cancer Cell. 2009; 15:35–44. [PubMed: 19111879]

10. Peinado H, Lavotshkin S, Lyden D. The secreted factors responsible for pre-metastatic niche formation: old sayings and new thoughts. Semin Cancer Biol. 2011; 21:139–146. [PubMed: 21251983]

11. Sleeman JP. The metastatic niche and stromal progression. Cancer Metastasis Rev. 2012; 31:429–440. [PubMed: 22699312]

12. Qian B, et al. A distinct macrophage population mediates metastatic breast cancer cell extravasation, establishment and growth. PLoS One. 2009; 4:e6562. [PubMed: 19668347]

13. Gabrilovich DI, Nagaraj S. Myeloid-derived suppressor cells as regulators of the immune system. Nat Rev Immunol. 2009; 9:162–174. [PubMed: 19197294]

14. Hiratsuka S, Watanabe A, Aburatani H, Maru Y. Tumour-mediated upregulation of chemoattractants and recruitment of myeloid cells predetermines lung metastasis. Nat Cell Biol. 2006; 8:1369–1375. [PubMed: 17128264]

15. Sceneay J, et al. Primary tumor hypoxia recruits CD11b+/Ly6Cmed/Ly6G+ immune suppressor cells and compromises NK cell cytotoxicity in the premetastatic niche. Cancer Res. 2012; 72:3906–3911. [PubMed: 22751463]

16. Qian BZ, et al. CCL2 recruits inflammatory monocytes to facilitate breast-tumour metastasis. Nature. 2011; 475:222–225. [PubMed: 21654748]

17. Lee J, et al. Implantable microenvironments to attract hematopoietic stem/cancer cells. Proc Natl Acad Sci USA. 2012; 109:19638–19643. [PubMed: 23150542]

18. Moreau JE, et al. Tissue-engineered bone serves as a target for metastasis of human breast cancer in a mouse model. Cancer Res. 2007; 67:10304–10308. [PubMed: 17974972]

19. Erez N, Coussens LM. Leukocytes as paracrine regulators of metastasis and determinants of organ-specific colonization. Int J Cancer. 2011; 128:2536–2544. [PubMed: 21387299]

20. Solinas G, Marchesi F, Garlanda C, Mantovani A, Allavena P. Inflammation-mediated promotion of invasion and metastasis. Cancer Metastasis Rev. 2010; 29:243–248. [PubMed: 20414701]

21. Yoneda T, Williams PJ, Hiraga T, Niewolna M, Nishimura R. A bone-seeking clone exhibits different biological properties from the MDA-MB-231 parental human breast cancer cells and a brain-seeking clone in vivo and in vitro. J Bone Miner Res. 2001; 16:1486–1495. [PubMed: 11499871]

22. Yi J, Backman V. Imaging a full set of optical scattering properties of biological tissue by inverse spectroscopic optical coherence tomography. Opt Lett. 2012; 37:4443–4445. [PubMed: 23114323]

23. Fujimoto JG. Optical coherence tomography for ultrahigh resolution in vivo imaging. Nat Biotechnol. 2003; 21:1361–1367. [PubMed: 14595364]

24. Huang D, et al. Optical coherence tomography. Science. 1991; 254:1178–1181. [PubMed: 1957169]

25. Yi J, et al. Can OCT be sensitive to nanoscale structural alterations in biological tissue? Opt Express. 2013; 21:9043–9059. [PubMed: 23571994]

26. Backman V, Roy HK. Advances in biophotonics detection of field carcinogenesis for colon cancer risk stratification. J Cancer. 2013; 4:251–261. [PubMed: 23459690]

27. Nadiarnykh O, LaComb RB, Brewer MA, Campagnola PJ. Alterations of the extracellular matrix in ovarian cancer studied by Second Harmonic Generation imaging microscopy. BMC Cancer. 2010; 10:94. [PubMed: 20222963]

28. Radosevich AJ, et al. Ultrastructural alterations in field carcinogenesis measured by enhanced backscattering spectroscopy. J Biomed Opt. 2013; 18:97002.

29. Turzhitsky V, et al. Investigating population risk factors of pancreatic cancer by evaluation of optical markers in the duodenal mucosa. Dis Markers. 2008; 25:313–321. [PubMed: 19208949]

30. Yi J, et al. Spatially resolved optical and ultrastructural properties of colorectal and pancreatic field carcinogenesis observed by inverse spectroscopic optical coherence tomography. J Biomed Opt. 2014; 19:36013. [PubMed: 24643530]

31. Stypula-Cyrus Y, et al. HDAC up-regulation in early colon field carcinogenesis is involved in cell tumorigenicity through regulation of chromatin structure. PLoS One. 2013; 8:e64600. [PubMed: 23724067]

32. Ko CY, et al. The use of chemokine-releasing tissue engineering scaffolds in a model of inflammatory response-mediated melanoma cancer metastasis. Biomaterials. 2012; 33:876–885. [PubMed: 22019117]

33. Davis ME, et al. Injectable self-assembling peptide nanofibers create intramyocardial microenvironments for endothelial cells. Circulation. 2005; 111:442–450. [PubMed: 15687132]

34. Yu J, et al. The effect of stromal cell-derived factor-1alpha/heparin coating of biodegradable vascular grafts on the recruitment of both endothelial and smooth muscle progenitor cells for accelerated regeneration. Biomaterials. 2012; 33:8062–8074. [PubMed: 22884813]

35. Lim WH, et al. Stent coated with antibody against vascular endothelial-cadherin captures endothelial progenitor cells, accelerates re-endothelialization, and reduces neointimal formation. Arterioscler Thromb Vasc Biol. 2011; 31:2798–2805. [PubMed: 22015656]

36. Zhang W, et al. VEGF and BMP-2 promote bone regeneration by facilitating bone marrow stem cell homing and differentiation. Eur Cell Mater. 2014; 27:1–12. [PubMed: 24425156]

37. Shi C, et al. Stem-cell-capturing collagen scaffold promotes cardiac tissue regeneration. Biomaterials. 2011; 32:2508–2515. [PubMed: 21227504]

38. Gower RM, et al. Modulation of leukocyte infiltration and phenotype in microporous tissue engineering scaffolds via vector induced IL-10 expression. Biomaterials. 2014; 35:2024–2031. [PubMed: 24309498]

39. Graham JG, et al. PLG scaffold delivered antigen-specific regulatory T cells induce systemic tolerance in autoimmune diabetes. Tissue Eng Part A. 2013; 19:1465–1475. [PubMed: 23432371]

40. Jang JH, Rives CB, Shea LD. Plasmid delivery in vivo from porous tissue-engineering scaffolds: transgene expression and cellular transfection. Mol Ther. 2005; 12:475–483. [PubMed: 15950542]

41. Yap WT, et al. Collagen IV-modified scaffolds improve islet survival and function and reduce time to euglycemia. Tissue Eng Part A. 2013; 19:2361–2372. [PubMed: 23713524]

42. Yu S, et al. Tumor exosomes inhibit differentiation of bone marrow dendritic cells. J Immunol. 2007; 178:6867–6875. [PubMed: 17513735]

43. Hiratsuka S, Watanabe A, Aburatani H, Maru Y. Tumor-mediated upregulation of chemoattractants and recruitment of myeloid cells predetermines lung metastasis. Nat Cell Biol. 2006; 8:1369–1375. [PubMed: 17128264]

44. Talmadge JE, Gabrilovich DI. History of myeloid-derived suppressor cells. Nat Rev Cancer. 2013; 13:739–752. [PubMed: 24060865]

45. Vakoc BJ, et al. Three-dimensional microscopy of the tumor microenvironment in vivo using optical frequency domain imaging. Nat Med. 2009; 15:1219–1223. [PubMed: 19749772]

46. Rogers JD, Capoglu IR, Backman V. Nonscalar elastic light scattering from continuous random media in the Born approximation. Opt Lett. 2009; 34:1891–1893. [PubMed: 19529738]

47. Radosevich AJ, Yi J, Rogers D, Backman V. Structural length-scale sensitivities of reflectance measurements in continuous random media under the Born approximation. Opt Lett. 2012; 37:5220–5222. [PubMed: 23258058]

48. Rogers JD, Radosevich AJ, Yi J, Backman V. Modeling light scattering in tissue as continuous random media using a versatile refractive index correlation function. IEEE Journal of Selected Topics in Quantum Electronics. 2014; 20

49. Yi J, et al. Can OCT be sensitive to nanoscale structural alterations in biological tissue? Opt Express. 2013; 21:9043–9059. [PubMed: 23571994]

50. Dull T, et al. A third-generation lentivirus vector with a conditional packaging system. J Virol. 1998; 72:8463–8471. [PubMed: 9765382]
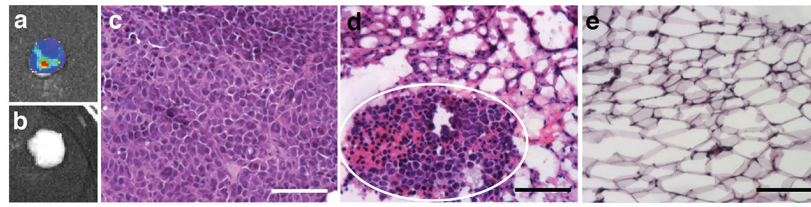
Figure 1. PLG scaffolds recruit metastatic tumor cells
Tissues were isolated at day 28 post-tumor inoculation (21 days after scaffold implantation or mock surgery). (**a,b**) Bioluminescence imaging (BLI) of peritoneal fat pads receiving scaffold implants (**a**) or mock surgeries (**b**). (**c–e**) Hematoxylin and eosin (H&E) staining of the primary tumor (**c**), a fat pad containing a scaffold (white circle indicates metastatic cluster) (**d**), and a fat pad without a scaffold (**e**). Scale bars indicate 100 μm.
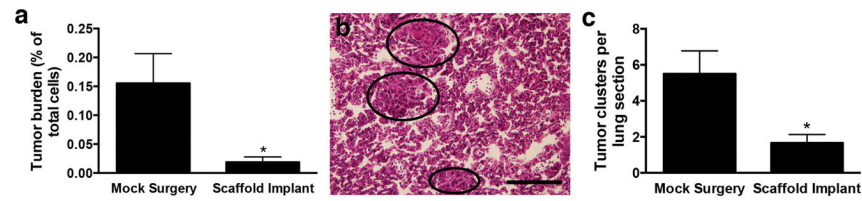
Figure 2. Recruitment of tumor cells to scaffolds reduces tumor burden in lung
(**a**) Flow cytometric analysis of the percentage of tdTomato-positive tumor cells in cells isolated from lungs at day 28 post-tumor inoculation. Data shown as mean ± SEM ($n = 8$, 2 independent replicates). * $P < 0.01$ compared to mock surgery (Mann-Whitney test). (**b**) H&E staining of lung section (which circles indicate metastatic clusters). Scale bar indicates 200 μm. (**c**) Histological analysis of H&E-stained lung sections to determine the number of tumor clusters per section. Data shown as mean ± SEM ($n = 12$, 2 independent replicates). * $P < 0.05$ compared to mock surgery (Mann-Whitney test).
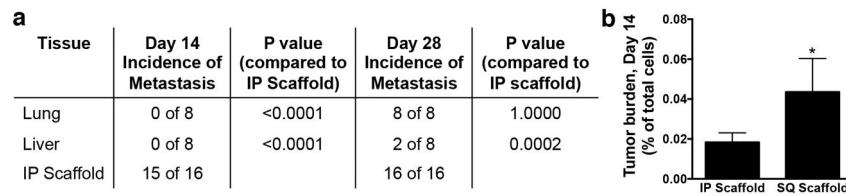
a

Tissue	Day 14 Incidence of Metastasis	P value (compared to IP Scaffold)	Day 28 Incidence of Metastasis	P value (compared to IP scaffold)
Lung	0 of 8	<0.0001	8 of 8	1.0000
Liver	0 of 8	<0.0001	2 of 8	0.0002
IP Scaffold	15 of 16		16 of 16	

b

Figure 3. Early detection of tumor cells in scaffolds

Flow cytometric analysis of tdTomato-positive tumor cells in tissues isolated from mice at day 14 and 28 post-tumor inoculation. (**a**) Number of mice with tumor cells detectable in each tissue in a group of 8 mice at day 14 or 28 post-tumor inoculation. Each mouse received two intraperitoneal (IP) scaffolds. P values from Fisher's exact test. (**b**) Percentage of tdTomato-positive cells in the total cell population isolated from IP scaffolds and subcutaneous (SQ) scaffolds at day 14 post-tumor inoculation. Data shown as mean ± SEM ($n = 16$ for IP scaffold, $n = 10$ for SQ scaffold, 2 independent replicates). * $P < 0.05$ compared to IP scaffold (Mann-Whitney test).
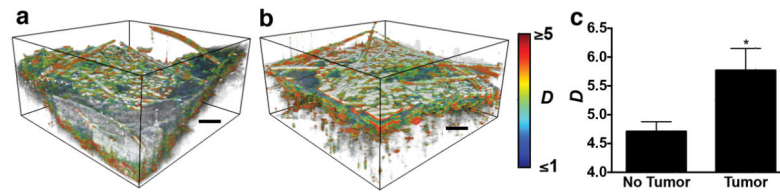
Figure 4. Detection of tumor cells in scaffold using IS-OCT

(**a,b**) Representative 3-D maps of *D* generated from *in situ* IS-OCT analysis of subcutaneous scaffolds implanted in tumor-free (**a**) and tumor-bearing (**b**) mice at day 14 post-tumor inoculation. Scale bars indicate 200 μm. (**c**) Average *D* value for subcutaneous scaffolds in tumor-free ("No Tumor") and tumor-bearing ("Tumor") mice. Data shown as mean ± SEM (*n* = 6, 2 independent replicated). * P < 0.05 compared to tumor-free mice (Mann-Whitney test).
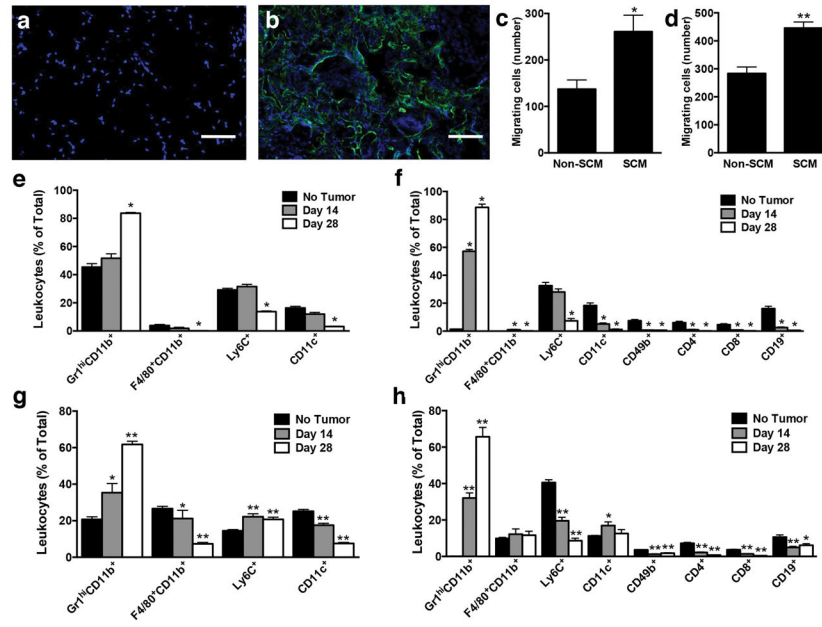
Figure 5. Evaluation of the immune environment within scaffolds
(**a,b**) CD-45 immunolabeling (green) at day 28 post-tumor inoculation of fat pads receiving mock surgery (**a**) or scaffold implant (**b**). Nuclei are blue. Scale bar indicates 100 μm. (**c,d**) Number of migrating 231BR (**c**) or 4T1 (**d**) cells in the presence of splenocyte-conditioned media (SCM) or non-conditioned media (non-SCM). Data shown as mean ± SEM (n = 6, 2 independent replicates). * P < 0.05 and ** P < 0.005 compared to non-conditioned media (Mann-Whitney test). (**e–h**) Flow cytometric analysis of cells removed from lungs (**e,f**) and scaffolds (**g,h**) of tumor-free and tumor-bearing (Day 14 and Day 28) NSG (**e,g**) or BALB/c (**f,h**) mice. The model used for mice with tumors involved the inoculation of cells at day 0, with scaffolds implanted at day 7. The evaluation of scaffolds in tumor free mice was performed following day 7 post-implantation. Cell populations are reported as percentage of total CD45-positive leukocytes. Data shown as mean ± SEM (n = 5 for lungs, n = 10 for scaffolds, 2 independent replicates). * P < 0.05 and ** P < 0.005 compared to Day 0 (**e,f**) or Day 14 (**g,h**) (Mann-Whitney test).
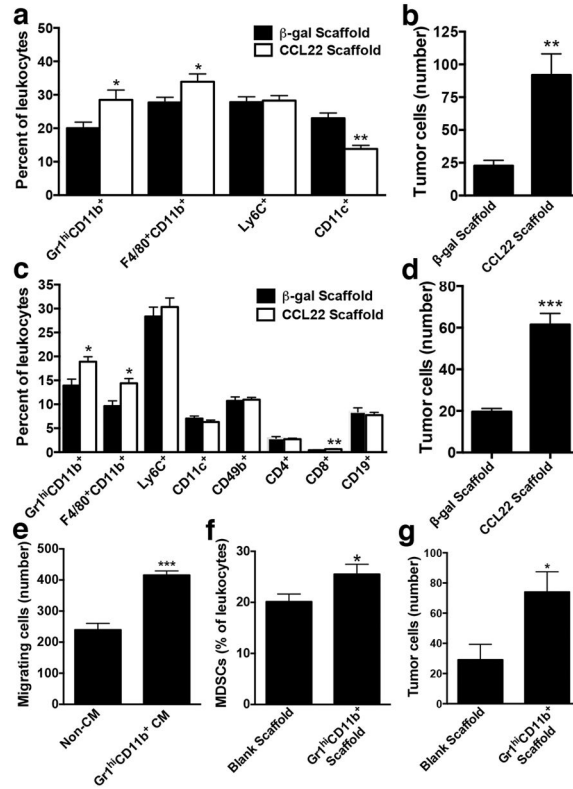
Figure 6. Immunomodulation of the scaffold microenvironment influences recruitment of tumor cells

Flow cytometric analysis at day 14 post-tumor inoculation of cells removed from scaffolds containing a CCL22 or β-galactosidase (control) vector implanted in NSG (**a,b**) or BALB/c (**c,d**) mice. Cell populations are reported as percentage of total CD45-positive leukocytes (**a,c**) or total number of tumor cells in the scaffold (**b,d**). Data shown as mean ± SEM ($n =$ 10, 2 independent replicates). * $P < 0.05$, ** $P < 0.005$ and *** $P < 0.001$ compared to β-galactosidase scaffolds (Mann-Whitney test). (**e**) Number of migrating 231BR cells in the presence of $Gr1^{hi}CD11b^{+}$ cell-conditioned media ($Gr1^{hi}CD11b^{+}$-CM) or non-conditioned media (non-SCM Data shown as mean ± SEM ($n = 6$, 2 independent replicates). *** $P <$ 0.001 compared to non-conditioned media (Mann-Whitney test). (**f,g**) Flow cytometric analysis at day 14 post-tumor inoculation of cells removed from blank scaffolds or scaffolds seeded with $Gr1^{hi}CD11b^{+}$ cells. Cell populations are reported as the percentage of $Gr1^{hi}CD11b^{+}$ cells in the total leukocyte population (**f**) or total number of tumor cells in the scaffold (**g**). Data shown as mean ± SEM ($n = 10$, 2 independent replicates). * $P < 0.05$ compared to blank scaffold (Mann-Whitney test).